Chapter-05: Melt-Spinning of Alloys

5.1 Introduction

Metallic glasses (MGs) are noncrystalline materials produced by rapid cooling a melt to suppress crystallization[193]. The Au-Si binary metallic alloys was the first composition made in 1960 by Duwez and his co-workers at Caltech[194] as metallic glass. MGs with distinct physical and chemical properties have led to a wide range of research for different applications[195], [196]. The requirement of an extremely high cooling rate (10^6-10^7 K/s) to produce metallic glass by melt-spinning limits the thickness of the sample[197]. Owing to this, the usage of glassy alloys as structural elements is still restricted[198]. Among various glass-forming alloys, Fe-based glassy alloys have attracted attention in this regard due to their high strength, stiffness, corrosion, wear resistance and magnetic properties[15], [198].

Glass forming ability (GFA) is an important terminology in the area of metallic glasses, and this indicates the easiness of glass transition and resistance to crystallization of the glassy phase[199]. Various GFA indicators, such as T_{rg}[200], ΔT_x[201], α, β, δ[202], [203] and γ[16], have been proposed in the literature. All these indicators are based on characteristic temperatures, such as melting temperature (T_m), glass transition temperature (T_g) and crystallization temperature (T_x) of the glassy alloys. The physical and mechanical properties of MGs can be improved by making nanocomposites. The nanocrystalline phases can be dispersed in the MG matrix. The researchers have been trying to optimize the microstructure through the design of nano MG composites so that the optimum combination of properties can get[117], [162], [204]. The microstructure depends on the alloy composition, cooling rate, melt flow position and wedge angle[193]. Fe-B-Si-based melt-spun ribbons have found uses in transformer core applications[205]. Jia et al.[206], produced Fe-based metallic glass ribbons for electro-catalytic application. They have used MG ribbons directly as electrodes without polymer binders and without losing the intrinsic conductivity. Yiu et al.[207], demonstrated a novel way of electro-plastic deformation of a Fe-based glassy ribbon for industrial scale fabrication of simple to complex geometry components.

The present work deals with the synthesis of four Fe-based glass/nanocomposites by melt-spinning technique from the alloys which are produced by Cu-mould casting as discussed in Chapter 4. The present work aims to investigate the microstructure and phase evolution in melt-spun ribbons. The micro-indentation behaviour of melt-spun ribbons was studied. The load-independent hardness

behaviour and yield strength of ribbons are reported. The formations of shear bands in all four compositions of ribbons are observed.

5.2 Experimental Procedures

Four ribbons with different compositions were synthesized by induction melting of alloy ingots which are produced by the Cu-mould casting technique (cf. chapter 4). Two different melt-spinning units were used to make ribbons. Alloy ingots of 5 to 7g quantity were sliced and placed in a crucible for melting. The complete information regarding the melt-spinner and specification of ribbons with designation are mentioned in Table 5.1. The nozzle of the crucible was aligned in such a way the melts flowed onto the rotating Cu-wheel when ejected. The Cu-wheel was water-cooled. The surface was finely polished before melt spinning. The crucible nozzle diameter was 0.5-3mm and the distance between the wheel and the crucible was 5-10mm. The ribbons were very brittle and could not be bent by 180^{o}. Figure 5.1 shows the optical image of synthesized ribbons with different wheel speeds. The maximum width up to ~7 mm was observed in MS-C at 3000 rpm. These ribbons were then vacuum sealed in a quartz tube (~20mm diameter) filled with argon atmosphere for annealing experiment.

Table 5. 1: Specifications of melt-spinner and melt-spun ribbons.

Melt-spun designation	**Crucible material**	**Wheel diameter(mm)**	**Wheel speed rpm**	**Average thickness (µm)**	**Average width(mm)**
MS-A	Quartz	300	2100	50	2
MS-B	Graphite	500	3000	33	5
MS-C	Graphite	500	3000	40	7
MS-C1	Quartz	300	1800	80	4
MS-D	Graphite	500	3000	20	2
MS-D1	Quartz	300	2100	40	2

Fig. 5. 1: Macroscopic images of melt-spun ribbons.

The microstructures of melt-spun ribbon samples were observed under an optical microscope (OM) (Leica model LV 500). The required size of alloys was taken for metallographic examination by following standard procedures for specimen preparation. The morphology of these samples was studied by scanning electron microscope (SEM) (Model: FEI Quanta 200F) operated at 30KV and equipped with an EDS detector. The investigation of structure and phases evolve in melt-spun ribbons was carried out by X-ray diffraction (HR-XRD EMPYREAN, PANALYTICAL) with Co-K_α (λ~1.78A^o) source, with 40 kV and 40mA operating voltage and current respectively. All the samples are cut in the required shape and put on the sample holder. Samples were scanned from

2θ=20 to 100^{o} angle. The interpretation of X-ray diffraction patterns was done with the help of a standard JCPDS/ICDD data source. Differential scanning calorimetry (DSC, 404 F3, and Pegasus Netzch) with a constant heating rate of 20^{o}C/min was used for the investigation of the crystallization of glassy alloys and also to know their thermal stability. Melt-spun ribbons were investigated by transmission electron microscopy (Tecnai G^2 T20) operated at 200kV. The TEM specimens of all four samples were prepared by grinding, dimpling and ion milling. The thinning of samples was done by precision ion milling using GATAN PIPS II. The samples were loaded at 6 degrees with 6keV operating voltage for 4 hours which was followed by 3 degrees with 3keV for half an hour and then 2 degrees with 2keV for again half an hour. The electron transparent region was first observed in the microscope attached to PIPS before loading into the TEM holder. The indentation characteristics are studied by an instrumented micro-hardness tester (Anton Parr: MHT^3). A Vickers diamond indenter was used. I have applied the indentation load from 10mN to up to fracture of the specimen with 20 sec of dwell time. At least ten indentations were done at each of the loads for reproducibility and averaging.

5.3 Results

5.3.1 Evolution of Microstructures

Figure 5.2 gives the optical micrographs of melt-spun ribbons. Ribbon samples were etched with 5% nital solution. The arrow marks show cracks which are developed during sample polishing. The microstructures show two types of features, irregular dark grey colour dots (shown in circle1) and light grey colour dots (shown in circle2). The phases present in them will become clear after the XRD results. The light grey colour dots, shown in circle2 are porosity in the sample which is developed during the melt-spinning process. Owing to a high level of perforations in the melt-spun ribbons the density of ribbons is not reported. The microstructures developed in all the melt-spun ribbons are similar.

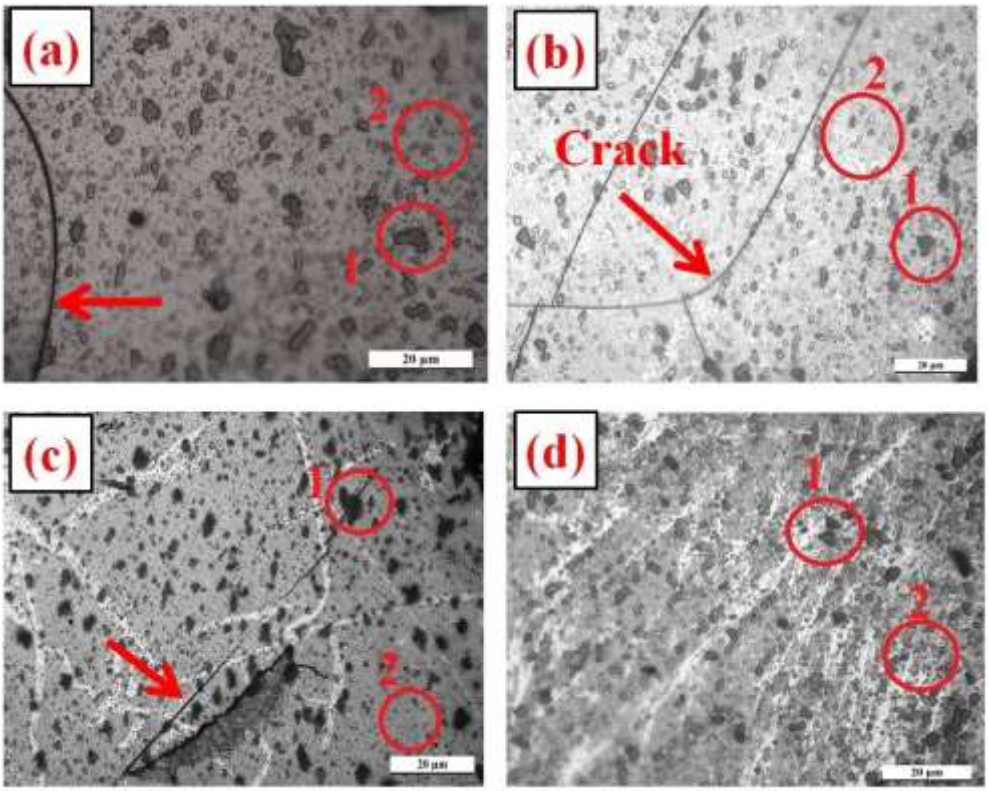

Fig. 5. 2: Optical image of melt-spun ribbon in etched condition (a) MS-A, (b) MS-B, (c) MS-C and (d) MS-D.

5.3.2 Structural and Phase Characterization: X-ray diffraction

Figure 5.3 depicts X-ray diffraction patterns of melt-spun ribbon MS-A in as-synthesized condition (fig. 5.3(a)) as well as heat-treated condition (fig.5.3 (b)). The XRD pattern of the as-synthesized ribbon of MS-A produced at wheel speed 2100rpm appeared to be amorphous, called X-ray amorphous[4]. The XRD patterns exhibit a broad diffuse maximum in the 2θ range of 51^o to 52^o and no traces of crystalline phases. The hump has its maximum intensity close to the d-spacing 2.06 A^o. When the sample is isothermally heated at 908K (near T_{X1}) for 1 hour, the XRD pattern displays multiple diffraction peaks instead of diffused halo. The d-spacing of the following crystalline phases matches with $Fe_{11}Mo_6C_5$ (mC44), α-Fe (cI2) and Fe_2B_7 (oP72) type of structures.

Similarly, the XRD pattern of melt-spun ribbon MS-B produced at wheel speed 3000rpm shows X-ray amorphous with a broad diffuse maximum in the 2θ range of 51^o to 52^o. The hump has its maximum intensity close to 2.08 A^o as shown in Fig. 5.4(a). The heat-treated sample of MS-B at a constant temperature of 908K for 1 hour, exhibits a diffuse maximum at the same 2θ position

and additionally a diffraction peak having d-spacing 3.08 A^{o}. The d-spacing of this peak is very close to $Fe_{11}Mo_6C_5$ phase.

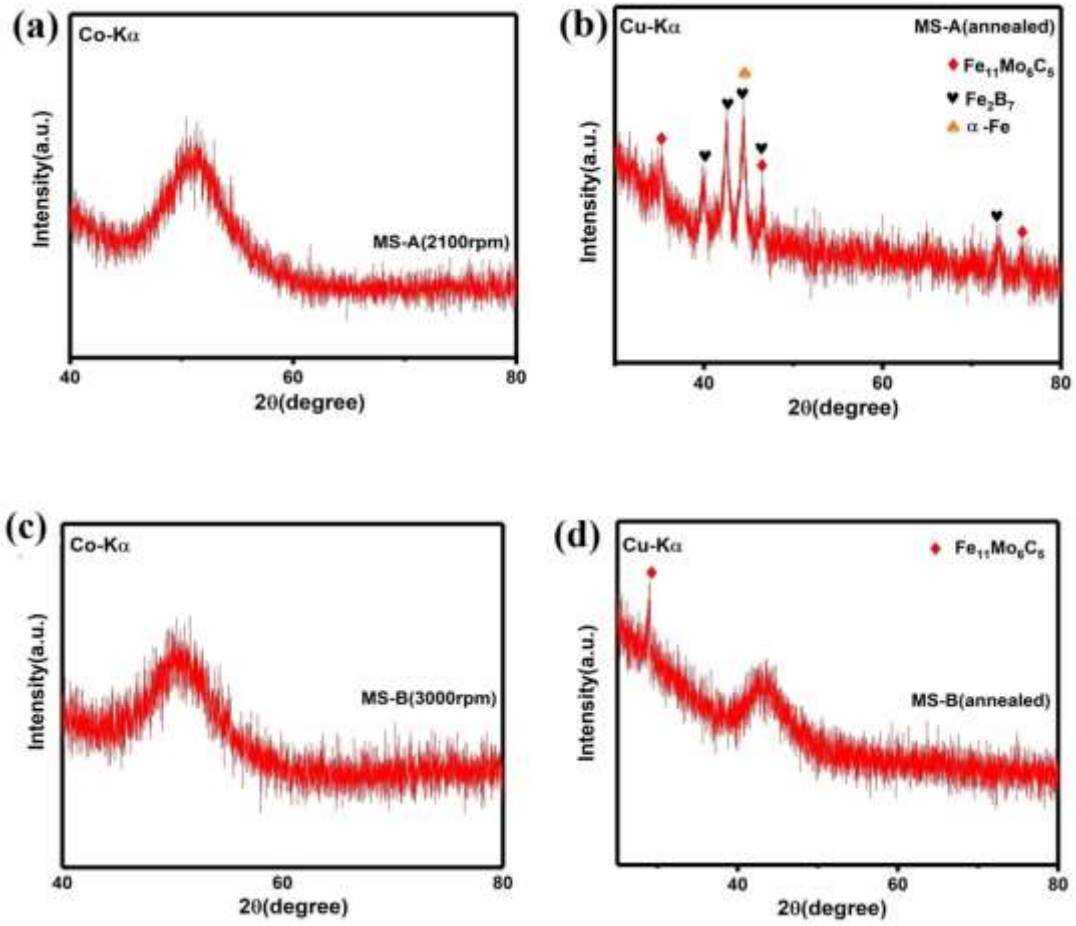

Fig. 5. 3: XRD pattern of melt-spun ribbons (a) as-synthesized MS-A, (b) annealed MS-A (at 908K for 1h), (C) as-synthesized MS-B and (d) annealed MS-B (at 908K for 1h).

Figure 5.4 (a) shows the XRD patterns of the free surface of melt-spun ribbon MS-C at different wheel speeds. It can be seen that sharp multiple crystalline peaks are observed when ribbon (MS-C1) was synthesized at 1800rpm wheel speed as shown in Fig. 5.4 (a(i)). The d-spacing of these crystalline peaks are very close to the following phases, $Fe_{11}Mo_6C_5$, Fe_3C, and α-Fe. However, with increasing wheel speed of the melt spinner (3000rpm), the crystalline peaks disappeared and the sample of MS-C exhibits diffused halo patterns, indicating the formation of an amorphous structure or X-ray amorphous as shown in Fig. 5.4(a(ii)). When the sample of MS-C (3000rpm) is heated at 918K for 1 hour, the XRD pattern displays a diffuse maximum at the same 2θ position

with the addition of a crystalline peak rising around diffuse halo as shown in fig.5.4 (b). The d-spacing of the crystalline peak matches with the d-spacing of $Fe_{11}Mo_6C_5$ and α-Fe phases.

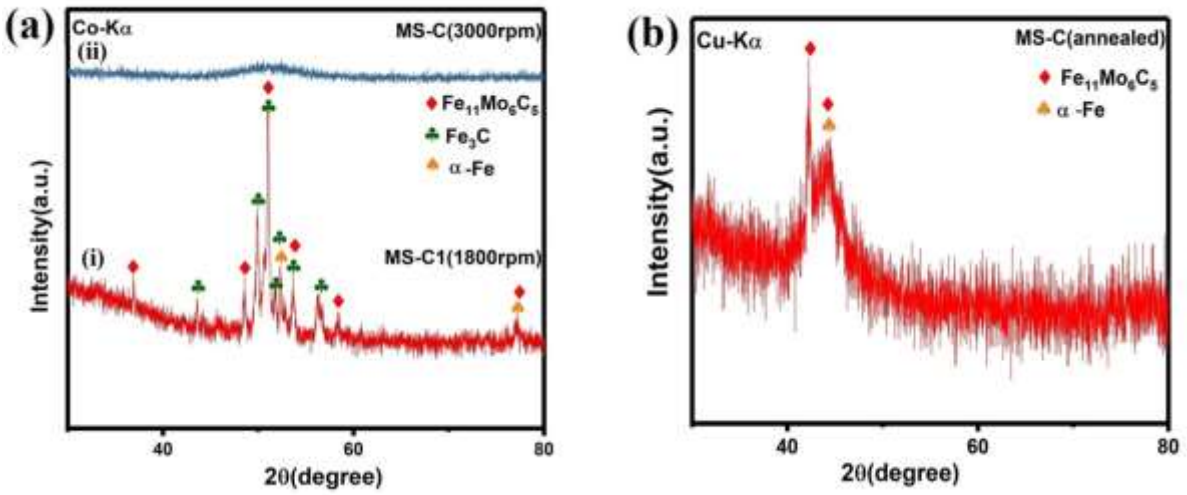

Fig. 5. 4: XRD pattern of melt-spun ribbon MS-C; (a) as-synthesized at different speed and (b) annealed ribbon (at 918K for 1h)**.**

The XRD pattern of melt-spun ribbon MS-D1, synthesized at 2100rpm wheel speed exhibits sharp crystalline peaks as shown in Fig. 5.5(a (i)). The d-spacing of these two peaks are 2.12 and 2.06 A^o, which are very close to $Fe_{11}Mo_6C_5$ (mC44) and α-Fe (cI2). When the wheel speed of the melt-spinner increases (i.e. 3000rpm), the crystalline peaks disappear and a broad diffused halo is formed (fig.5.5 a (ii)). The hump has its maximum intensity close to the d-spacing 2.06 A^o. Due to the formation of a diffused hump, indicating MS-D has an amorphous phase or X-ray amorphous is formed. The sample of melt-spun ribbon MS-D (3000rpm) was isothermally heated at 918K for 1 hour, the XRD pattern display sharp crystalline peaks (splitting type) at the same 2θ range where a diffused halo was formed. It is indicating that the coordination polyhedral of the noncrystalline and crystalline phases are similar. The d-spacing of these two crystalline peaks is very close to $Fe_{11}Mo_6C_5$ (mC44) and α-Fe (cI2) phase. The behaviour of X-ray amorphous of all melt-spun ribbons will be confirmed through a transmission electron microscope (TEM) in the next sub-section.

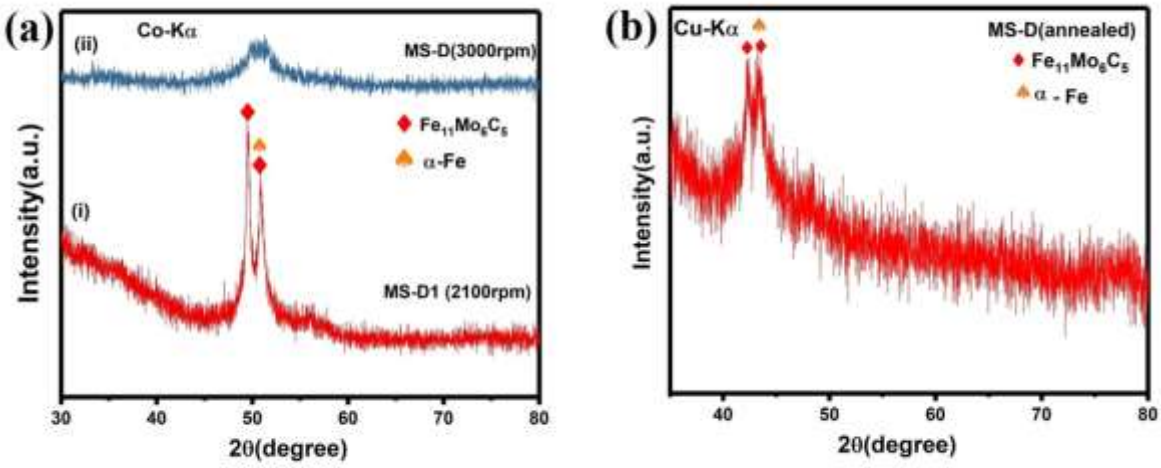

Fig. 5. 5: XRD pattern of melt-spun ribbon MS-D; (a) as-synthesized at different speeds and (b) annealed ribbon (at 918K for 1h)**.**

5.3.3 Phase Analysis: Transmission Electron Microscopy (TEM)

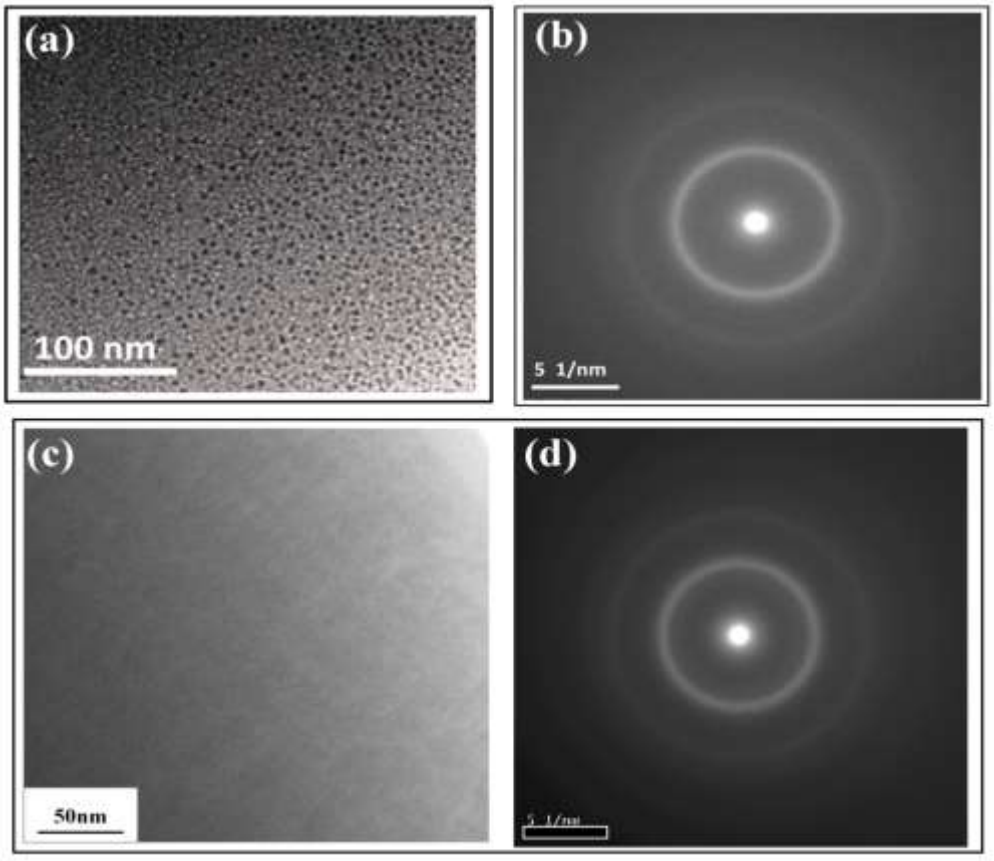

Fig. 5. 6: (a) and (c) Bright field (BF) image of melt-spun ribbons MS-A and MS-D with (b) and (d) corresponding diffraction patterns showing diffuse halos.

The XRD results of melt-spun ribbons show peak broadening which needs to be confirmed through TEM about its validity of forming an amorphous phase. The TEM bright field (BF) images of MS-A and MS-D are shown in Fig. 5.6 (a) and (c) respectively. It can be noted that the TEM bright field image displays no contrast and the corresponding diffraction pattern shows diffuse halos in Fig. 5.6 (b) and (d) respectively. These results permit one to infer the predominant formation of the amorphous phase in the observed regions.

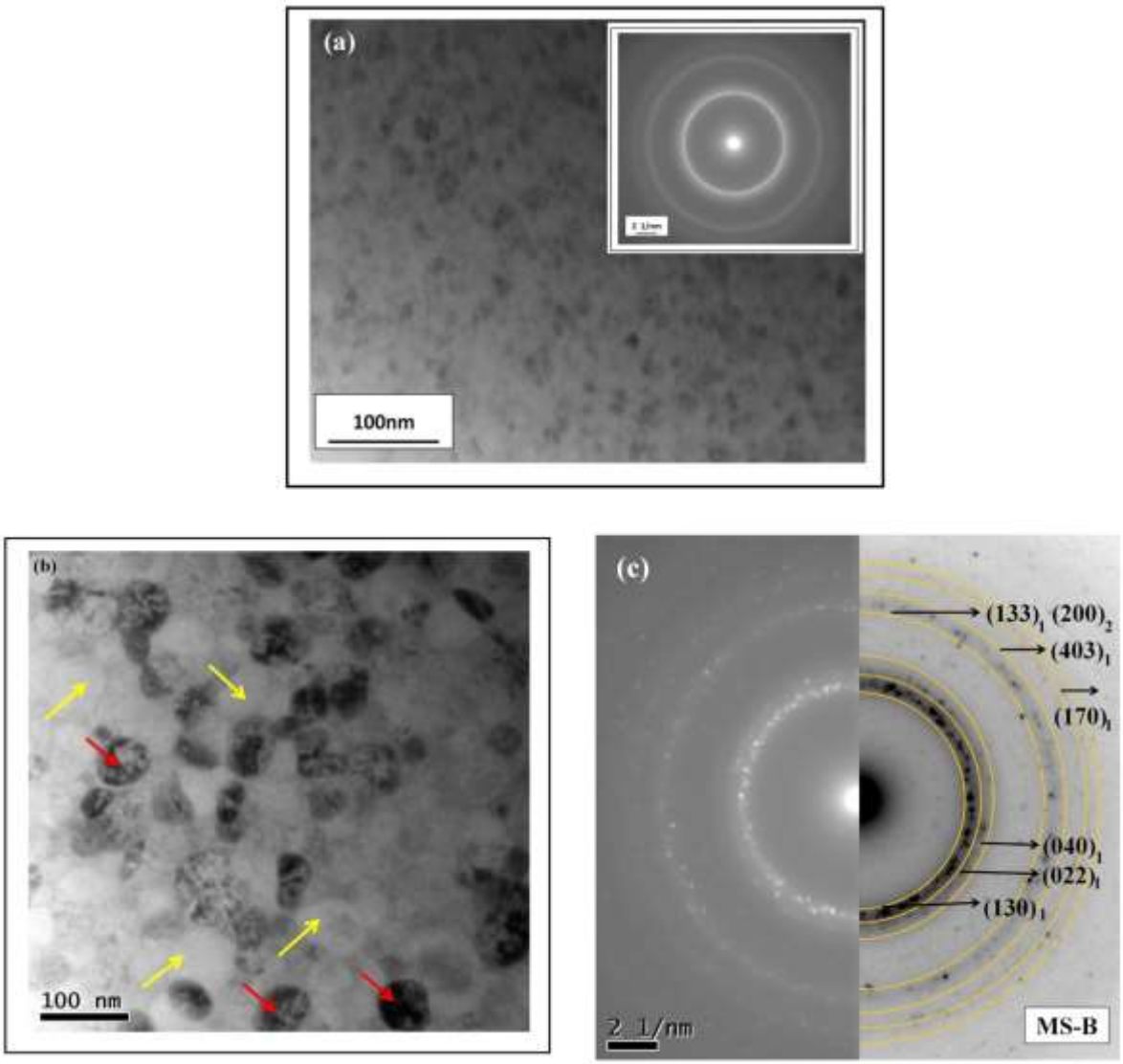

Fig. 5. 7: (a) Bright-field image of MS-B sample and inset shows corresponding diffraction pattern, (b) bright field image of the same sample from a different place, and (c) corresponding inverted diffraction pattern superimposed with actual diffraction pattern. 1→$Fe_{11}Mo_6C_5$; 2→α-Fe.

Figure 5.7(a) shows the bright field image of melt-spun ribbon MS-B and the inset showing the corresponding diffraction pattern. The diffraction pattern contains a continuous ring of diffused halo in some of the regions. Figure 5.7(b) represents the bright field image from different places of the same ribbon having three different contrasts. Figure 5.7 (c) shows Continuous polycrystalline rings that indicate the formation of the nanocrystalline phase. The black contrasts of nanocrystals have having grain size of ~ 45nm. In addition, diffraction spots are also seen. This continuous polycrystalline ring is a signature of fine grains. The diffraction halos, polycrystalline rings, and spots indicate the presence of crystalline phases embedded in the amorphous matrix. The indexing of the polycrystalline ring is given in the fig. 5.7(c). To quantitatively analysis of diffraction rings, yellow-colored semi-circular rings are superimposed onto the diffraction pattern as shown in Fig. 5.7(c). These d-spacing values are matches with either α-Fe (cI2) or $Fe_{11}Mo_6C_5$ (mC44) phases. The same phases have been observed in the XRD pattern of MS-B (cf. fig. 5.3(c)).

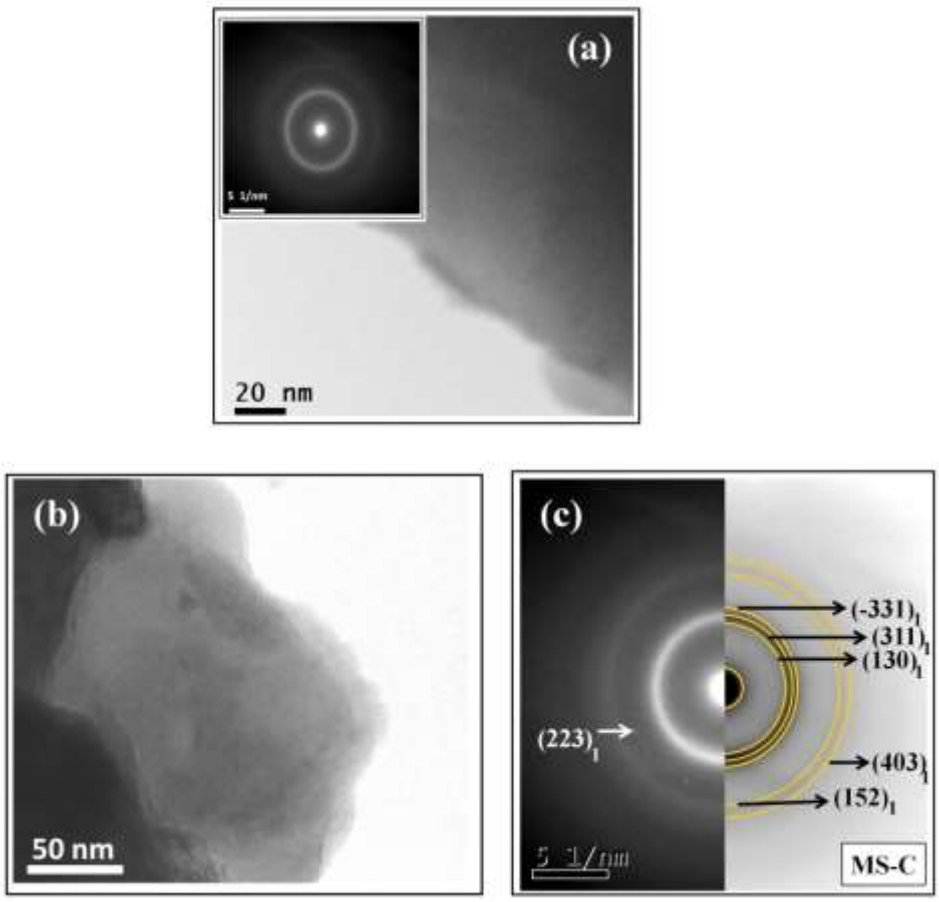

Fig. 5. 8: (a) Bright-field image of MS-C sample and inset shows corresponding diffraction pattern (b) bright field image from a different place of the same sample and (c) corresponding inverted diffraction pattern superimposed with actual diffraction pattern: 1→$Fe_{11}Mo_6C_5$

Fig.5.8 (a) represents the bright field image of MS-C and the inset shows the corresponding diffraction pattern. In a bright field image, there is no contrast. The diffraction pattern of MS-C shows diffused halos which is a signature of complete amorphization. For the same ribbon from a different region, the bright field image shown in Fig. 5.8 (b) and the corresponding diffraction pattern display diffused rings with crystalline spots as shown in Fig. 5.8 (c). The d-spacing of these spots and diffused rings match with the $Fe_{11}Mo_6C_5$ (mC44) phase.

5.3.4 Morphology of melt-spun ribbon

Figure 5.9 (a-c) represents the SEM images of melt-spun ribbon MS-A with the same magnification. Three different areas are chosen for EDS analysis. Full area, dark region (spot1), and grey region (spot2) are shown with the arrow marks in figs. 5.9 (a-c). The SEM-EDS spectrum at the full area, spot 1, and spot 2 are shown in Fig. 5.9 (d-f). The distributions of all the elements in a melt-spun ribbon of the MS-A sample are uniform and their compositions are shown in Table 5.2. Full area EDS-spectrum shows that Fe and Mo are rich in this area.

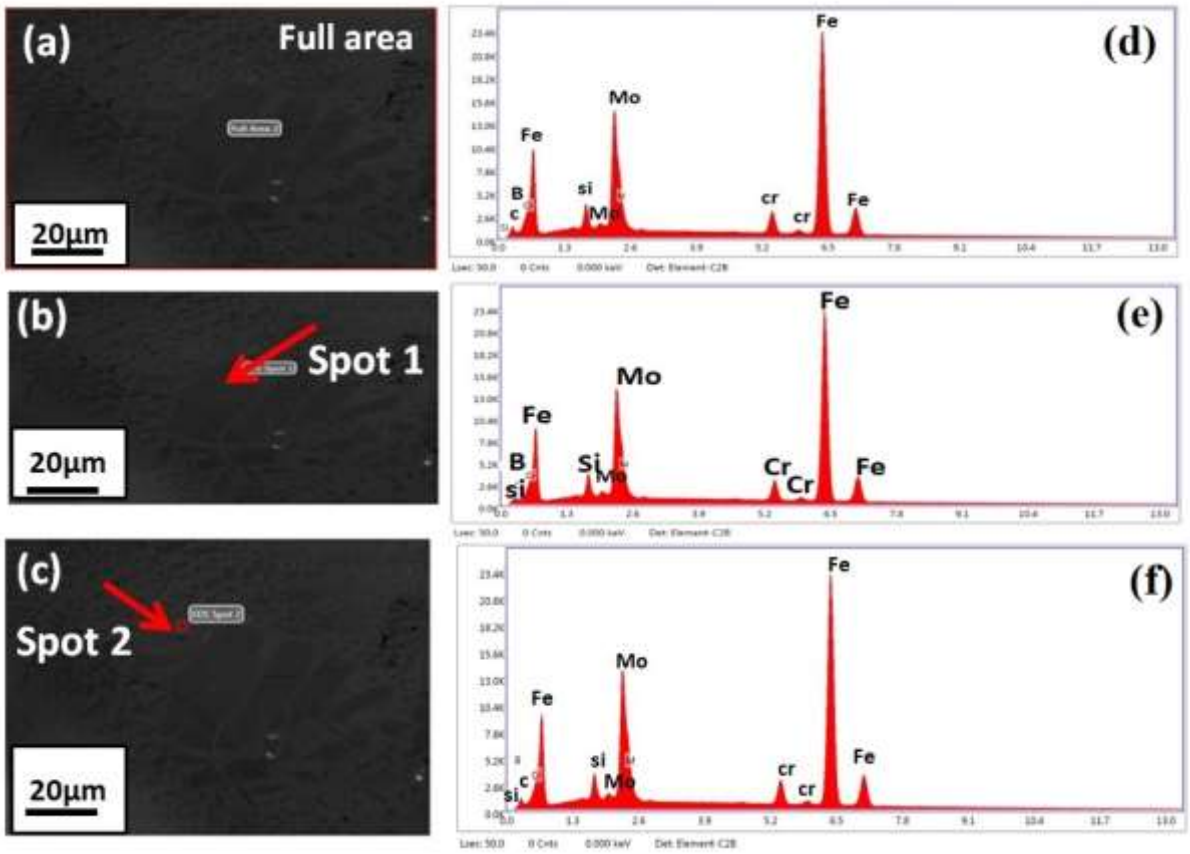

Fig. 5. 9: (a-c) SEM images of MS-A sample at the same magnification, showing full area, spot 1, and spot 2; (d-f) Energy dispersive spectra (EDS) of the marked area.

Spot 1 and Spot 2 are also rich in Fe and Mo. Therefore, due to uniformity in composition distribution that's why amorphous phase was observed in MS-A.

Table 5. 2: Elemental composition of MS-A sample by point EDS analysis.

Element	Full area	Spot-1	Spot-2
	at%	at%	at%
B	0	0	0
C	3.8	0.4	0.5
Si	4.2	2	1.9
Mo	14.2	22.8	22.7
Cr	5.8	5.3	5.2
Fe	72	69.5	69.7

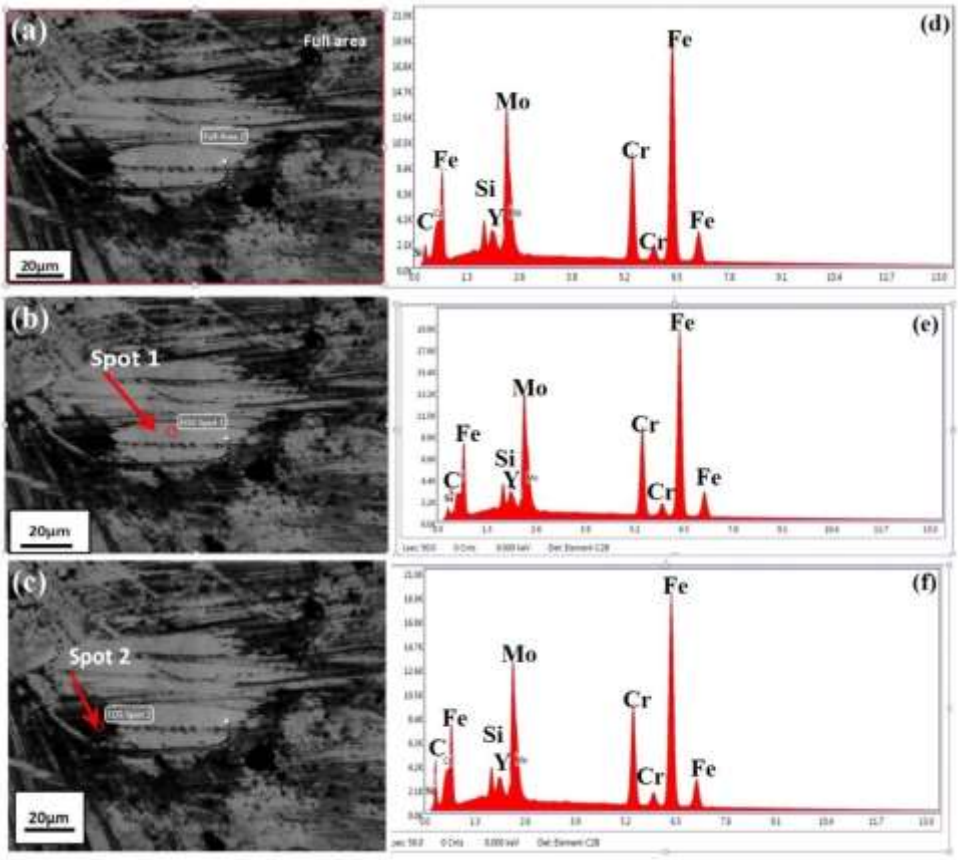

Fig. 5. 10: (a-c) SEM images of MS-B sample at the same magnification, showing full area, spot 1, and spot 2; (d-f) EDS spectrum of the marked area.

Two different contrasts are seen in the SEM micrograph of melt-spun ribbon MS-B as shown in Fig. 5.10 (a-c). Three different regions are chosen for SEM-EDS analysis. Full area, grey region (spot 1) and black region (spot 2) are shown in fig. 5.10(a-c) with arrow marks and corresponding EDS-spectrums are shown in fig. 5.10 (d-f). It was observed that the full area is rich in Fe, Cr, Mo, and C and the rest are present in lean amounts. The large grey area (i.e. spot 1) is rich in Fe, Cr, and Mo elements. The large black area (i.e. spot 2) is rich in Fe, C, and Cr. The distributions of all the elements in a melt-spun ribbon of the MS-B sample are non-uniform and their compositions are shown in Table 5.3. Therefore, due to the non-uniform distribution of compositions nanocrystalline phases are formed in the amorphous matrix (c.f. 5.7).

Table 5. 3: Elemental composition of MS-B sample by point EDS analysis.

Element	**Full area**	**Spot-1**	**Spot-2**
	at%	**at%**	**at%**
B	0	0	0
C	10	3.9	33.9
Si	3.6	3.9	2.7
Y	1.6	1.7	1.2
Mo	11.4	12.2	8.5
Cr	18.9	20.2	13.9
Fe	54.4	58	39.9

Figure 5.11 (a-c) shows the SEM micrograph of melt-spun ribbon MS-C at the same magnification. The SEM micrograph shows two different contrasts, grey color (matrix) and dark black spots. Three different regions were chosen for EDS analysis. Full area, dark black spot (spot 1), and grey color region (spot 2). It was observed that the full area is rich in Fe (~57 at %), Cr (20 at %), and Mo (~13 at %), and the rest are in lean. Spot 1 is rich in Fe (49.5 at %), Cr (~17.5 at %), and C (~17 at %). Spot-2 is rich in Fe (~58 at %), Cr (20.4 at %), and Mo (13.5 at %). The distributions of all elements are non-uniform and their compositions in at % are given in Table 5.4.

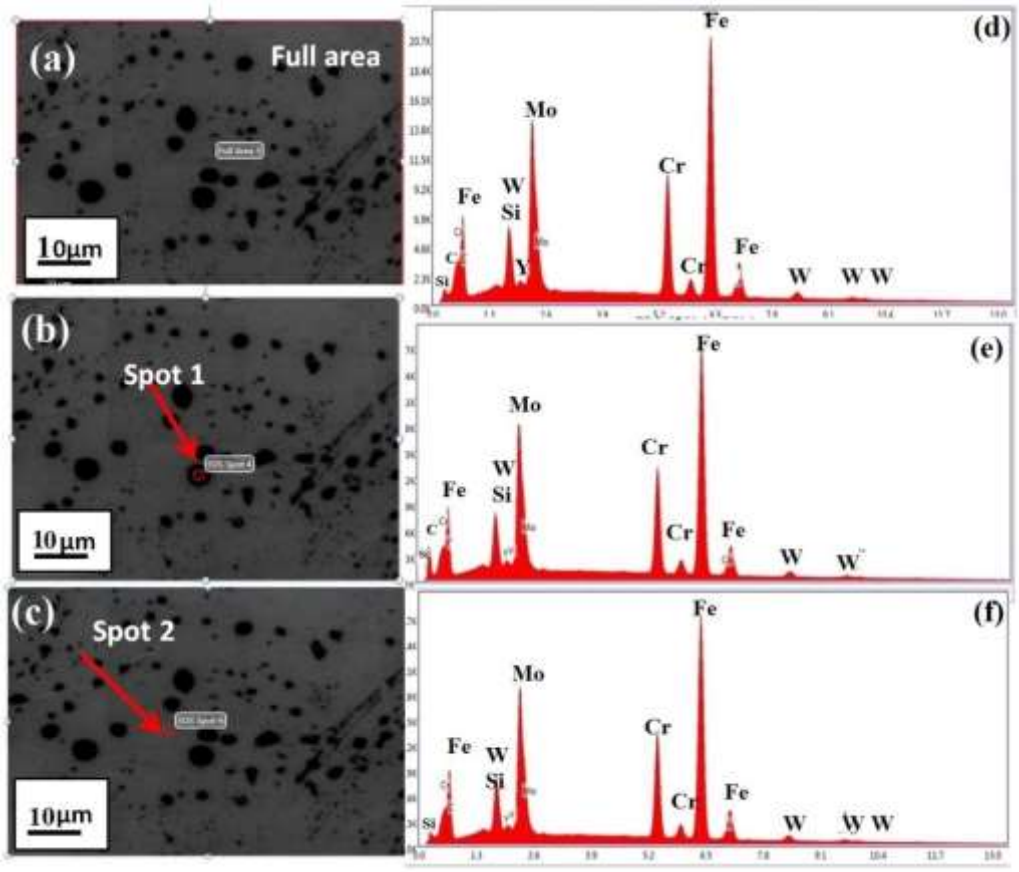

Fig. 5. 11: (a-c) SEM images of MS-C sample at the same magnification, showing full area, spot 1, and spot 2; (d-f) EDS spectrum of the marked area.

Table 5. 4: Elemental composition of MS-C sample by point EDS analysis

Element	Full area	Spot-1	Spot-2
	at%	at%	at%
B	0	0	0
C	3.7	16.9	2.6
Si	3.4	2.9	3.4
Y	0	0.3	0.4
Mo	13.4	11.5	13.5
Cr	20.1	17.4	20.4
Fe	56.9	49.5	57.8
W	2	1.7	2.3

The SEM micrograph of the melt-spun ribbon MS-D is shown in Fig. 5.12(a-c). It was observed that the melt-spun ribbon MS-D has a uniform microstructure. It has been seen that some white particles are distributed in the matrix. Three different areas were selected for EDS analysis. Full area, large white spot (spot 1), and small white spot (spot 2) are shown by arrow marks in Fig. 5.12 (a-c). It was observed that the full area is rich in Fe (~52 at %), Cr (~26 at %), and the rest are present in lean amounts. Spot 1 is rich in Fe (47 at %) and Cr (24.5 at %) and the rest are lean. Similarly, spot 2 is rich in Fe (~51 at %) and Cr (25.5 at %), and the rest elements are present in lean amounts. The distributions of all the elements in a melt-spun ribbon of MS-D sample are uniform and their compositions are shown in Table 5.5. It was observed from the EDS spectrum (fig. 5.12(d-f)) as well as from Table 5.5 that all the areas that have been selected for EDS analysis have almost the same composition. Therefore, uniform microstructures have been observed and that's why melt-spun ribbon MS-D shows complete amorphisity (c.f. fig.5.6 (c & d)).

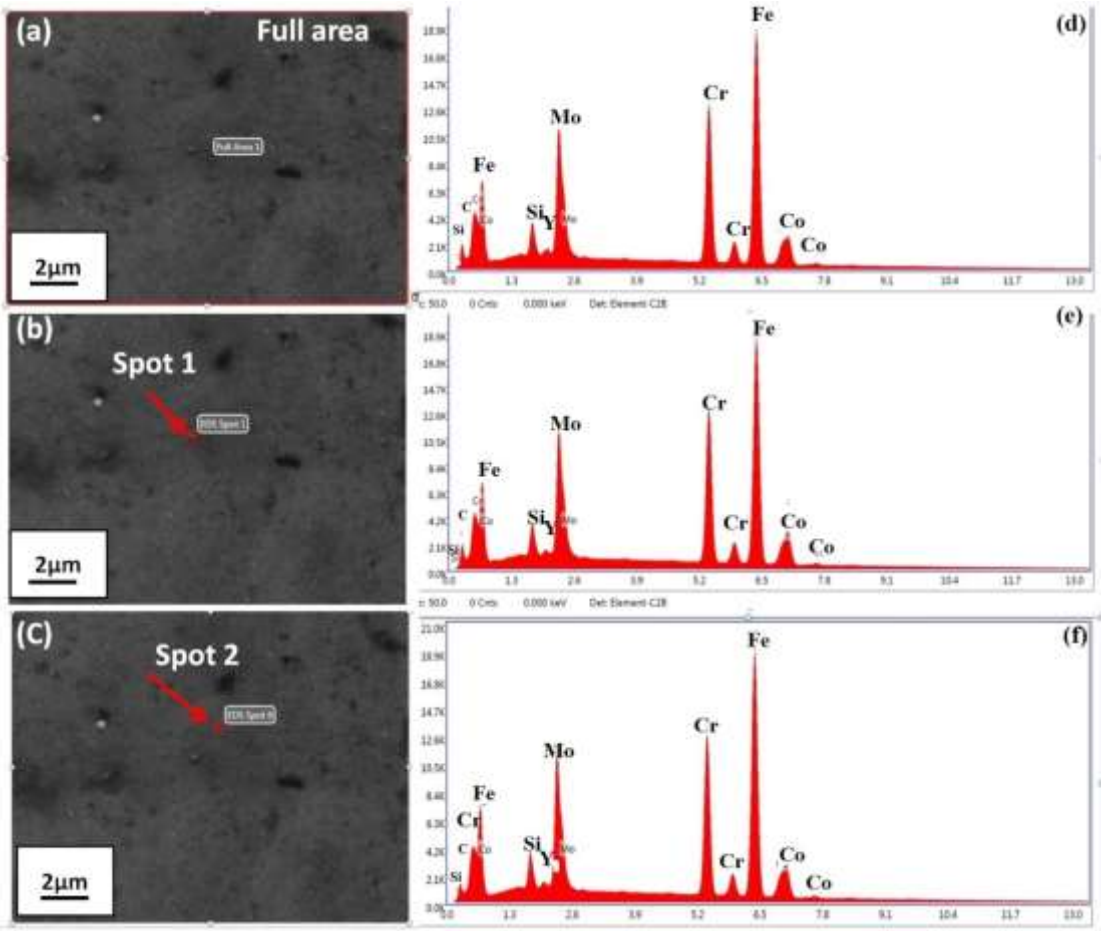

Fig. 5. 12: (a-c) SEM images of MS-D sample at the same magnification, showing full area, spot 1, and spot 2; (d-f) EDS spectrum of the marked area.

Table 5. 5: Elemental composition of MS-D sample by point EDS analysis.

Element	Full area	Spot-1	Spot-2
	at%	at%	at%
B	0	0	0
C	3.5	10.2	3.9
Si	3.9	3.6	3.9
Y	1.2	1.8	1.6
Mo	9.5	8.9	9.4
Cr	25.7	24.5	25.4
Fe	52.1	47.2	51.2
Co	4	3.7	4.4

5.3.5 Thermal Behaviour Analysis

DTA experiment was conducted with the heating rate of 20^{o}C/min and DSC thermographs are shown in Fig. 5.13 for melt-spun-ribbons samples. The results reveal that glass transition exhibits only in MS-A and MS-C as shown in Fig. 5.13(a) and (b) respectively. The multi-stage crystallization occurs in both samples. The thermal parameters like glass transition temperature ($T_{g)}$, crystallization temperatures (T_X), melting temperature (T_m), and peak temperature (T_p) are taken from the DTA scan and listed in Table 5.6. With the help of these values the super-cooled liquid region ΔTx (=Tx–Tg), reduced glass transition temperatures T_{rg1} (=T_g/T_m) and T_{rg2} (=T_g/T_l), gamma parameter 'γ' (=$T_x/(T_l+T_g)$ and delta parameter 'δ' (=$T_x/(T_l-T_g)$ were calculated for these two ribbons. These parameters are generally used to indicate thermal stability and GFA[158][208]. Among these two ribbons, the maximum super-cooled liquid region was found to be 60 ^{o}C for MS-A. It indicates that the thermal stability and GFA are found to be better in ribbon MS-A than in other ones.

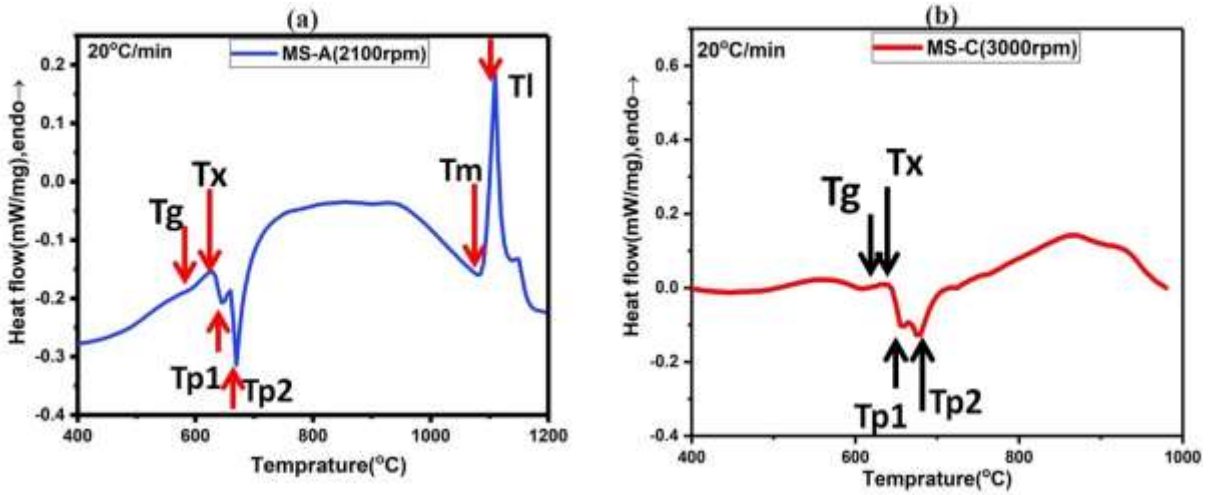

Fig. 5. 13: DTA thermogram of melt-spun ribbons, (a) MS-A, and (b) MS-C, with a heating rate of 20°C/min.

Table 5. 6: Thermal parameters by DTA scan of melt-spun ribbon samples at a heating rate of 20 °C/min. (all temperatures are in °C).

Melt-spun ribbons	Tg	Tx1	Tm	Tl	ΔTx1	Tx2	ΔTx2	Trg1	Trg2	Γ	δ
MS-A	600	625	1085	1110	25	660	60	0.55	0.54	0.36	1.22
MS-C	609	640	1140	1185	31	664	55	0.53	0.51	0.35	1.11

5.3.6 Nature of indentation of melt-spun ribbon at different load

Figures 5.14 (a-d) show the optical image of indentation impressions for melt-spun ribbons at various loads. The indentation impressions are crack-free up to a load of 100g in all the samples. It is to be noted that the initiation of cracks is observed at 300g, 200g, 300g, and 200g applied load in MS-A, MS-B, MS-C, and MS-D samples respectively as shown by the arrow marked. It was observed that cracks appeared later in MS-A and MS-C (at 300g) as compared to MS-B and MS-D (at 200g), which suggests that the sample of MS-A and MS-C has better toughness as compared to MS-B and MS-D. In the case of annealed ribbons, samples of MS-A and MS-B failed at 100g load, while samples of MS-C and MS-D failed at 200g of indentation load. Here cracks are not Palmqvist type. It was observed that the size of the indentation impression in all melt-spun ribbon

samples as shown in Fig. 5.15 (a-d), increases at a slower rate at low load but it drastically increases at high load conditions.

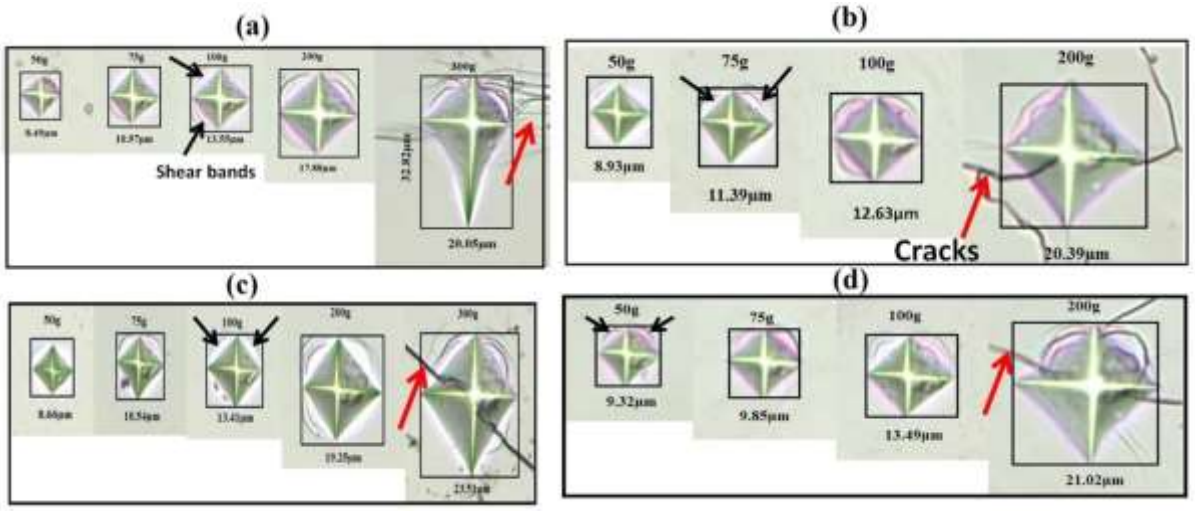

Fig. 5. 14: Optical images of indentation impression from various regions for as-synthesized ribbons (a) MS-A, (b) MS-B, (c) MS-C, and (d) MS-D, showing the nature of indentation with load up to fracture. Shear bands are formed around the indentation periphery and cracks are also observed.

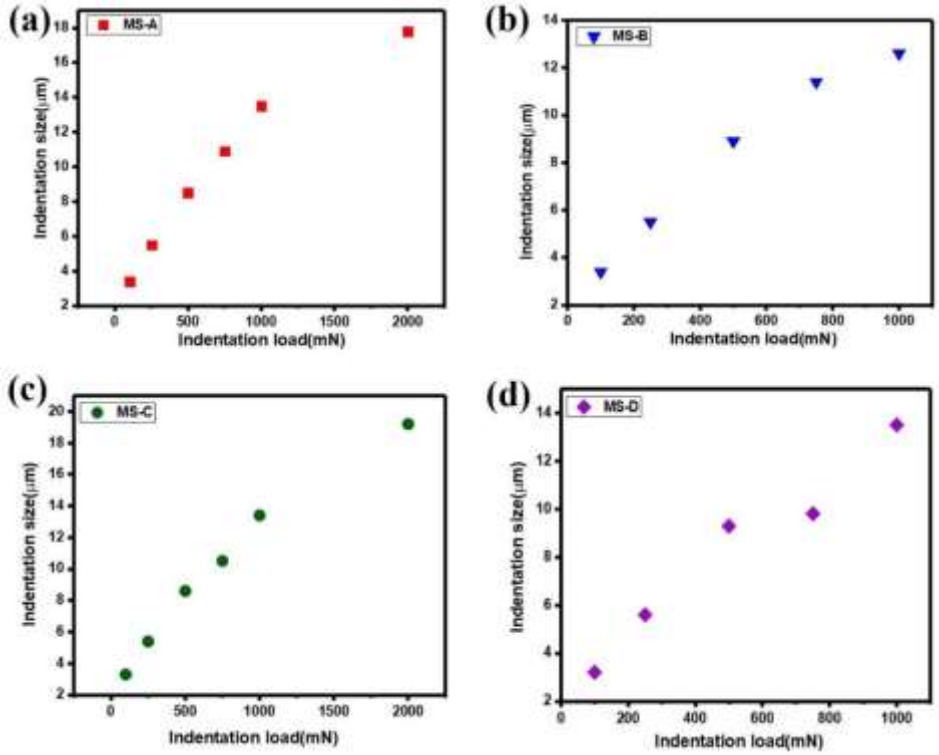

Fig. 5. 15: Shows the nature of variation of indentation size with load in (a) MS-A, (b) MS-B, (c) MS-C, and (d) MS-D.

Figures 5.16 (a-d) give the hardness versus load characteristics of melt-spun ribbons as well as partially crystallized (annealed) ribbons. It has been seen that in melt-spun ribbons the hardness value strictly depends on the applied load. Load-dependent hardness is owing to the indentation size effect (ISE)[209]. Similarly, after partial crystallization of melt-spun ribbons i.e. annealed ribbons show ISE for MS-A, MS-B, MS-C, and MS-D. However, it can also be observed from fig. 5.17 that the annealed ribbon sample displays a sharper reduction of hardness with indentation depth as compared with amorphous/nanocrystalline ribbons. The microhardness values of melt-spun ribbons as well as annealed samples at various loads are given in Table 5.7.

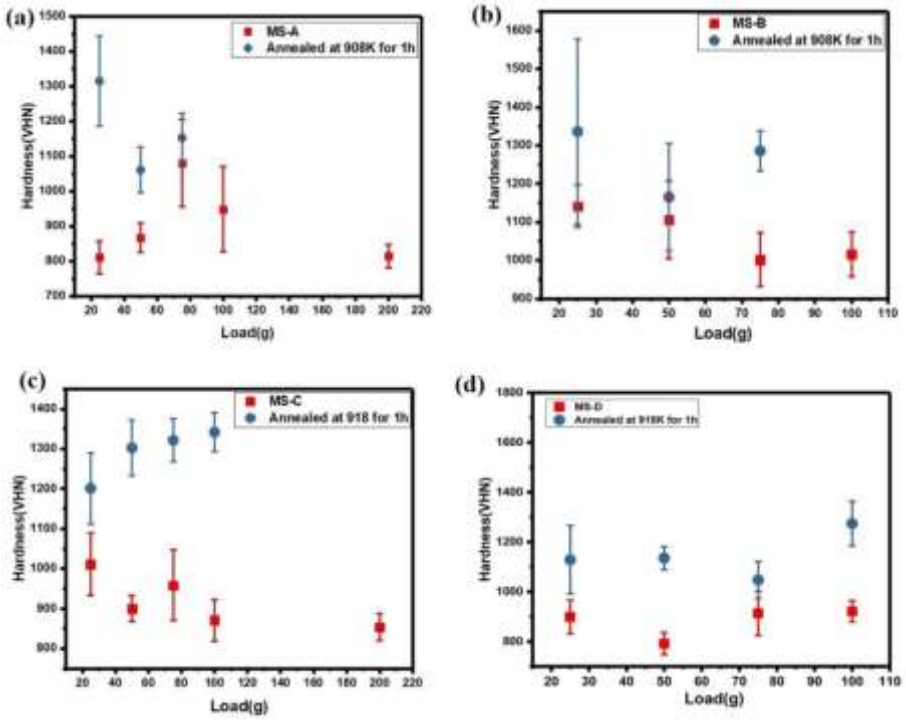

Fig. 5. 16: Variation of hardness (VHN) for the load (g) for the melt-spun ribbons ribbon and annealed ribbons of (a) MS-A, (b) MS-B, (c) MS-C, and (d) MS-D.

Table 5. 7: Microhardness data in GPa at various loads for melt-spun ribbons and annealed samples (AMS) are displayed. Later is indicated in boldface.

	Vickers hardness (H_V) with std. dev. (in GPa)				
Load(g)	**MS-A** **AMS-A**	**MS-B** **AMS-B**	**MS-C** **AMS-C**	**MS-D** **AMS-D**	**Remarks**
25	8.5±0.5 **14±1**	8±0.6 **14±2**	10.5±1 **12.5±1**	9.5±0.7 **12±1.5**	No crack **No crack**
50	9±0.5 **11±0.7**	8±0.8 **12±1**	9.5±0.3 **14±1**	8.5±0.5 **12±0.5**	No crack **No crack**
75	11.5±1.3 **12±0.8**	7.5±0.5 **13.5±0.5**	10±1 **14±0.5**	9.5±1 **11±0.8**	No crack **No crack**
100	10±1	8.5±0.5	9±0.6 **14±0.6**	9.5±0.5 **13.5±1**	No crack **Crack in A.S-A & A.S-B**
200	8.6±0.3		9±0.3		Cracks in MS-B, MS-D, A.S-C, & A.S-D

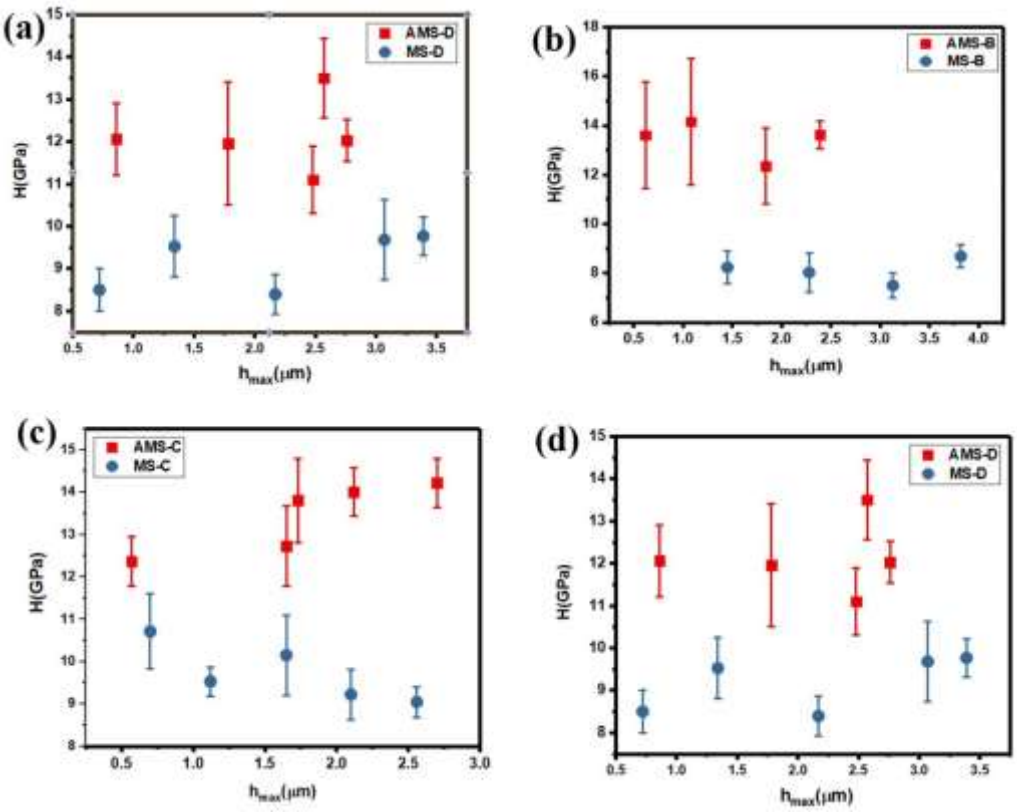

Fig. 5. 17: Dependence of the indentation hardness on depth (maximum) for melt-spun ribbons (MS) and annealed ribbons (AMS).

Among all the melt-spun ribbons, MS-A has a maximum average hardness value of ~10GPa at 100g indentation load and a maximum average elastic modulus of ~50GPa. In the case of annealed ribbons, the maximum average hardness was found in MS-C and its value is ~14 GPa at 75g of indentation load.

A comparative study has been done at 75g of indentation load among all the as-synthesized ribbons and annealed ribbons as shown in Fig. 5.18. The microhardness values of these samples are given in Table 5.7. It has been observed that at 75g of applied load MS-A has maximum hardness (~11.5 GPa), while in the case of annealed ribbons MS-C has maximum hardness value (14 GPa).

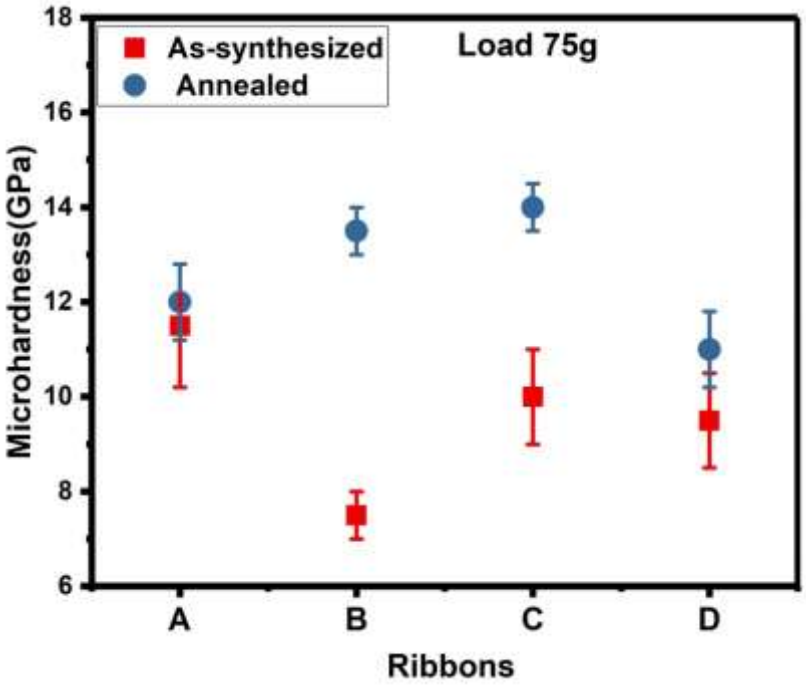

Fig. 5. 18: Comparison of hardness (GPa) at indentation load of 75g among all the melt-spun ribbons (as-synthesized) and annealed ribbons.

5.3.7 Determination of Yield strength (σ_o), Meyer's exponent (n), material constant (K)

The 0.2% offset yield strength of the melt-spun ribbon samples can be calculated from microhardness measurements using the following expression[173][189]:

$$\sigma_o = (VHN/3)0.1^{n-2}$$

Where σ_o = 0.2% offset yield strength and n is Meyer's exponent and related to the material capacity of work hardening. The variation of hardness with load can be analyzed using Meyer's law[173]. The variation of load related to the diagonal length (d) as:

$$P = Kd^n$$

Where P is the applied load (in Kg), d is the indentation diagonal length (in mm), K is the material constant related to the resistance of the metal to penetration and n is Meyer's exponent or Meyer's index. The value of n can be calculated from a plot of LogP versus Logd. The slope of the line gives the value of n. The value of n varies from material to material. From the present experimental data, the LogP vs Logd curves for melt-spun ribbon samples has been plotted and shown in Fig. 5.19. The values of Meyer's exponent (n) and LogK are given in Table 5.8. It has been observed that the value of 'n' lies in the range of 1.7 to 2. The Meyer's

Table 5. 8: Values of average VHN, E, n, Log K, and σ_o of melt spun ribbons at 75g load**.**

Melt-spun ribbons	VHN (GPa) (75g load)	Reduced Elastic modulus (E)(GPa)	n	LogK	σ_o (GPa) (75g load)	VHN/σ_o
MS-A	11.5	58	1.84	2.48	5.54	2.07
MS-B	7.5	41	1.70	2.18	4.98	1.50
MS-C	10	65	1.80	2.37	5.28	1.89
MS-D	9.5	44	2.0	2.97	3.16	3.0

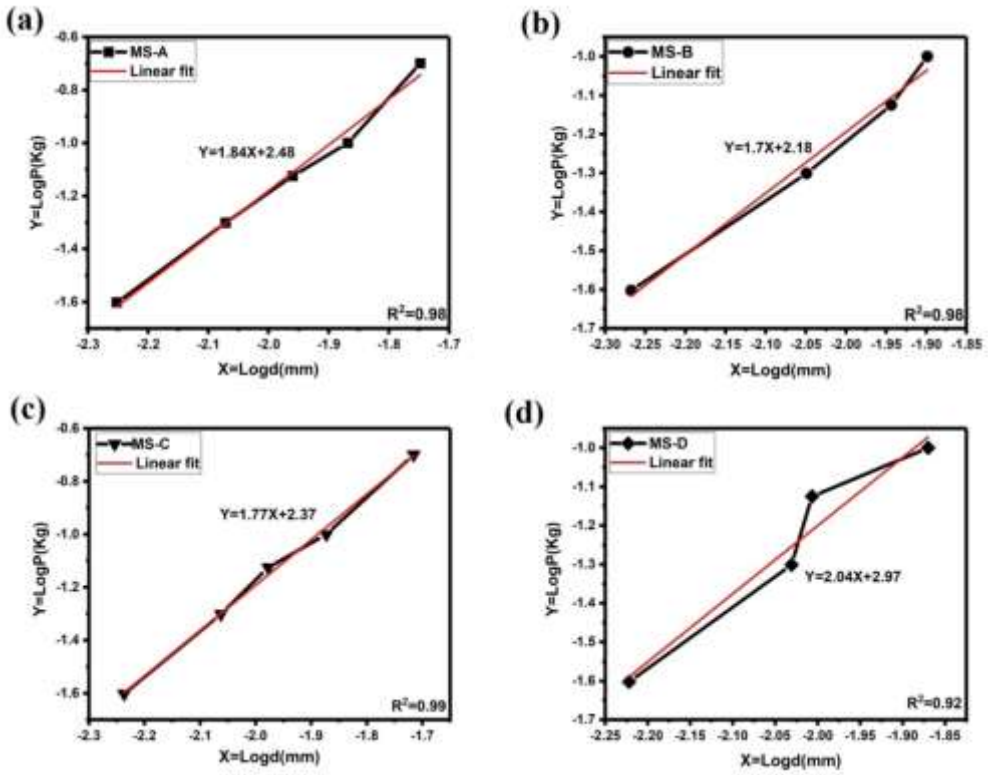

Fig. 5. 19: Log P vs Log d plots for melt-spun ribbon samples, (a) MS-A, (b) MS-B, (c) MS-C, and (d) MS-D. The lines are the linear fit to the data and R^2 is the correlation coefficient and has a value in the range 0.92-0.99.

exponent values for all the melt-spun ribbon samples are found to be different. This change is due to microstructural and structural variations in them, as different alloying additions have been taken. The value of Meyer's exponent is less than 2, which has been observed for intermetallic by Mukhopadhyay et al.[210]. It has been observed that σ_o is the maximum for MS-A (~5.5GPa)

among all the melt-spun ribbons. The Meyer's exponents is maximum for MS-D (~2) and also the ratio of VHN/σ_o is highest for MS-D (=3).

5.3.8 Determination of Plastic criterion (R_w) and Percentage of Elastic recovery (%R)

The load-displacement (P-h) curves for melt-spun ribbons as well as annealed melt-spun ribbons (AMS) are shown in Fig. 5.20 (a) and (b) at a load of 75g. The maximum depth of penetration (h_{max}) for the melt-spun ribbons A, B, C, and D are found to be 2.74, 3.17, 2.49, and 2.95µm respectively. In the case of annealed melt-spun ribbons, the maximum depth of penetration for AMS-A, B, C, and D are found to be 2.63, 2.59, 2.10, and 2.45µm respectively. The net amount of work done during an indentation test can be estimated by the area enclosed by the p-h curve. The indentation experiment also provides a way to estimate the magnitude of deformation (elastic or plastic). Three important parameters were calculated from the P-h curves for melt-spun ribbons

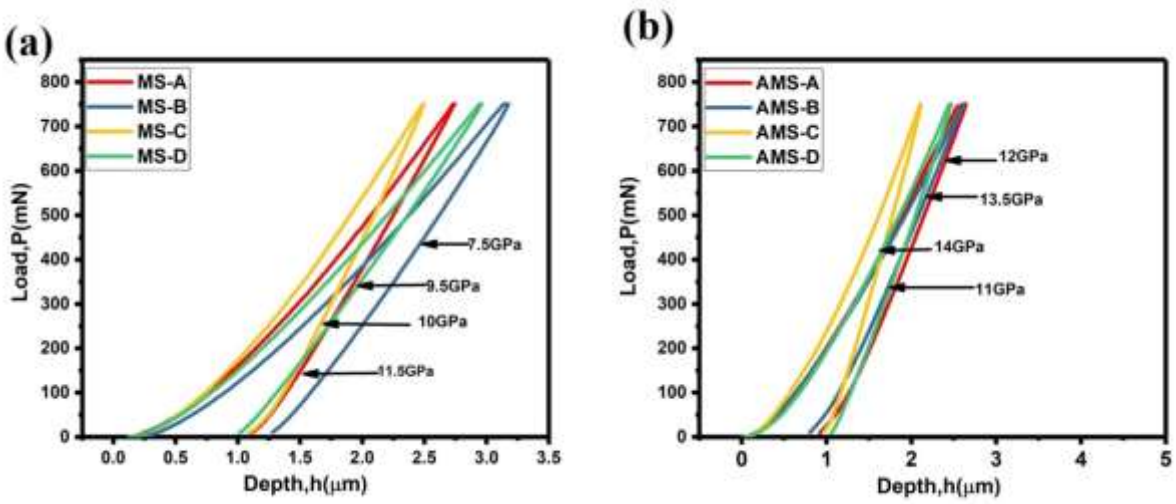

Fig. 5. 20: Load-displacement (P-h) plot of (a) melt-spun ribbons and (b) annealed ribbons (AMS) at 75g load.

as well as for annealed samples. These parameters are referred to (i) A plastic criterion (R_w)[178][179], (ii) elastic recovery (R)[211] and (iii) Percentage of elastic recovery rate (%R)[211].The following expressions are used to find these parameters for melt-spun ribbons as well as annealed ribbons.

(i) $$\% R_W = \frac{WP}{WT} x\ 100$$

(ii) **Elastic recovery, $R = h_f/h_{max}$**

(iii) $$\%R = \frac{(hmax - hf)}{hmax} X100\%$$

Table 5. 9: The Mechanical properties of the tested melt-spun ribbons estimated from the P-h plot at 75g indentation load

Melt-spun ribbon	W_P (10^{15} J)	W_e (10^{15} J)	W_T (10^{15} J)	R_W (in %)	h_f (μm)	h_{max} (μm)	R (h_f/h_{max})	%R
MS-A	198	577	776	25.5	1.11	2.74	0.40	60
MS-B	295	671	966	30.5	1.27	3.19	0.39	61
MS-C	253	909	1162	22	1.08	2.50	0.43	57
MS-D	217	953	1350	29	1.02	2.90	0.35	65

Table 5. 10: The Mechanical properties of the tested annealed melt-spun ribbons were estimated from the P-h plot at 75g indentation load.

Annealed ribbon	W_P (10^{15} J)	W_e (10^{15} J)	W_T (10^{15} J)	R_W (in %)	h_f (μm)	h_{max} (μm)	R (h_f/h_{max})	%R
AMS-A	243	551	794	30.6	0.93	2.63	0.35	65
AMS-B	196	800	996	19.7	0.77	2.59	0.29	71
AMS-C	245	427	672	36.5	0.98	2.11	0.46	54
AMS-D	246	475	721	34	1.05	2.45	0.42	57

The parameter R_w is calculated for melt-spun ribbons and annealed ribbons and it is found to be in the range of ~ (22-40%) and ~ (19-40%) respectively. This result indicates that elastic deformation due to indentation is more as compared to plastic deformation in the materials in both cases. MS-B and AMS-C have a maximum value of R_w i.e. ~30.5% and 36.5% respectively. This result shows that MS-B and AMS-C have a good amount of plasticity among all samples. The elastic recovery values of melt-spun ribbons and annealed ribbons are in the similar range of 0.3 to 0.5. The values of all these relevant parameters as described above for melt-spun ribbons and annealed ribbons are given in Table 5.9 and Table 5.10 respectively.

The ratio of hardness to elastic modulus (H/E) also known as the degree of elastic recovery is calculated for the melt-spun ribbons and annealed ribbons and their values are given in Table 5.11. It has been observed from Table 5.11 that the H/E ratio of melt-spun ribbon is found to be in the range of (0.15-0.21) and for annealed ribbons in the range of (0.15-0.28).

Table 5. 11: Some important Mechanical properties of melt-spun ribbons and annealed ribbons at 75g load.

Melt-spun ribbons	**H (GPa)**	**E (GPa)**	**H/E**	**Annealed ribbons**	**H (GPa)**	**E (GPa)**	**H/E**
MS-A	11.5	58	0.20	AMS-A	12	64	0.18
MS-B	7.5	41	0.18	AMS-B	13.5	47	0.28
MS-C	10	65	0.15	AMS-C	14	90	0.15
MS-D	9.5	44	0.21	AMS-D	11	72	0.15

5.4 Discussion

5.4.1 Microstructure, Phase/Structure Analysis

The microstructures developed in all the melt-spun ribbons are similar. A high level of perforation is present in the melt-spun ribbon which is why the density of ribbons is not measured.

The change in melt-spinning process parameters (like wheel speed) can affect the cooling rate and consequently the structure of rapidly quenched alloys. It has been discussed in several papers and

reviews[212]–[214]. In this chapter, the phases or structures that evolve due to changes in wheel speed of rapidly quenched or melt-spun ribbons were studied. The XRD results of melt-spun ribbons confirmed that MS-A, MS-B, MS-C, and MS-D have given rise to produced X-ray amorphous[4] at a wheel speed of 2100rpm for MS-A and at 3000rpm for others. On the other hand, MS-C and MS-D evolved multiple crystalline peaks at wheel speeds of 1800rpm and 2100 rpm respectively. The phases evolved in MS-C1 (1800rpm) are $Fe_{11}Mo_6C_5$ (mC44), Fe_3C (oP116), and α-Fe (cI2), while in the case of MS-D1 (2100rpm), only $Fe_{11}Mo_6C_5$ (mC44) and α-Fe (cI2) phases are evolved. It was noticed that at low wheel speed (i.e. at low cooling rate), the crystallization process enhanced more quickly. Higher wheel speed conveys a larger cooling rate which restrains the atomic diffusion that suppresses the crystallization process. As a result, it is favorable to obtain an amorphous phase at high quenching wheel speed[214]–[216].

After the heat treatment (annealing) process of t melt-spun ribbon of MS-A, MS-B, MS-C, and MS-D, the XRD pattern displays multiple diffraction peaks instead of diffused halo. Most of the phases are common in all heat-treated ribbons except MS-A. In the case of MS-A, a new phase Fe_2B_7 was detected. The common phases are $Fe_{11}Mo_6C_5$ and α-Fe.

The X-ray results were confirmed through TEM observations. From TEM studies, it was confirmed that MS-A and MS-D have shown better glass-forming whereas, MS-B and MS-C have displayed amorphous-crystalline phases. The nanocrystalline phases of α-Fe and $Fe_{11}Mo_6C_5$ are embedded in an amorphous matrix of melt-spun ribbons in the latter two samples. All these are concluded based on the limit of TEM observations.

5.4.2 Thermal Analysis

The GFA of these ribbons has been described in terms of ΔT_x, T_{rg}, γ, and δ-parameters. Chen et al.[208], reported these thermal parameters for some ferrous and non-ferrous-based BMGs. The thermal parameters ΔT_x, T_{rg}, and γ values are comparable with those reported for Fe-based systems. Fe-based compositions for the Fe-Cr-Mo-C-B system were reported by Gu et al. [148] having values of these thermal parameters ΔT_x, T_{rg}, γ, and δ are 50K, 0.45, 0.34, and 0.91respectively. It is clear from Table 4 that all the parameters of the present metallic glass are higher than those reported by Gu et al. The thermal parameters T_g, T_x, ΔT_x, and T_{rg} of the present composition of MS-C are higher than those reported by Liang et al.[122], for Fe-Cr-Mo-W-C-B-Y system. Shen et al.[123], and Lu et al.[16], have reported ΔT_x and γ to be important parameters for the estimation of GFA of Fe-based alloys. In the present investigation, the super-cooled liquid

regions are to be achieved 60K and 55K for melt-spun ribbons MS-A and MS-C respectively. The high value of T_g and ΔT_x suggests the high thermal stability of the present alloys.

5.4.3 Indentation Characteristics Analysis

The Vickers micro-indentation experiment was carried out for the investigation of the nature of indentation for the as-synthesized ribbons as well as for annealed ribbons. Load-dependent hardness was observed in both conditions, i.e. as-synthesized ribbons as well as annealed ribbons. This effect demonstrates a significant indentation size effect (ISE)[85], [217]. A more significant ISE has been observed in the annealed ribbons as compared to melt-spun ribbons. The annealed ribbon displays a sharper reduction of hardness with indentation depth. The maximum Vickers microhardness was observed in MS-A (~11.5 GPa) at 75g load, while after the heat treatment process, AMS-C exhibited maximum Vickers microhardness (~14GPa) at 75g indentation load among all the ribbons. After the heat treatment process, nanocrystalline phases were developed in the amorphous matrix, which may lead to high hardness in annealed ribbons[189]. The cracks were observed later in MS-A and MS-C at 300g load whereas for MS-B and MS-D, it was at 200g load. It suggests the sample of MS-A and MS-C has better toughness and more resistance to crack propagation as compared to MS-B and MS-D[189]. From the P-h curve of the melt-spun ribbon and annealed ribbon, it was observed that the maximum penetration depth (h_{max}) was found in MS-B (4μm) and AMS-D (~2.8μm). The 0.2 % offset yield strength (σ_o) was found maximum for MS-A (~5.5 GPa) at 75g load. The Meyer index (n) is calculated from exponential curve fitting of the indentation diagonal length d (mm) versus applied load P (kg) from a straight-line graph of log d versus log P. Meyer's index is a very useful parameter for work hardening and their value lies in the range of (1.7-2) for melt-spun ribbons. Sargent[175] stated that, if index $n < 2$, it is normal ISE. If $n > 2$, it is reverse ISE. If $n = 2$, the microhardness is independent of the load.

The area under the P-h curve provides a measure of the elastic and plastic energy component of deformation during indentation[177]. Three important parameters from the P-h plot were estimated. They refer to, (i) plastic criterion (R_w)[179], (ii) elastic recovery (R)[120] and percentage of elastic recovery (%R)[120]. The value of elastic recovery (h_f/h_{max}) for glass and Al are 0.68 and 0.95 respectively[120]. The elastic recovery limits in the present case are found to be in the range of (0.35-0.43) for melt-spun ribbons and (0.29-0.46) for annealed ribbons. The H/E ratio is maximum for MS-D (~0.21) and for AMS-B (0.28), it indicates that the elastic recovery is better in these two ribbons.

5.5 Conclusions

The microstructure, phase evolution, and indentation characteristics of four different alloy compositions processed through melt-spinning and after heat-treated samples were studied. The following important conclusions can be drawn from this part of the investigation:

(i) Four Fe-based alloy compositions were processed through the melt-spinning process. Amorphization takes place only in MS-A and MS-D. These two ribbons show better amorphous phase formation ability whereas MS-B and MS-C have displayed amorphous/nanocrystalline phase formation. The nanocrystallites of α-Fe (cI2) and $Fe_{11}Mo_6C_5$ (mC44) are embedded in an amorphous matrix.

(ii) The DTA scan of melt-spun ribbons exhibits the glass transition only in MS-A and MS-C. The GFA parameters (ΔT_x) and T_{rg}) of these samples suggest high thermal stability of the present alloys.

(iii) Both the samples of melt-spun ribbons and annealed ribbons show ISE. A more significant ISE has been observed in the annealed ribbon as compared to melt-spun ribbons.

(iv) The maximum microhardness value was observed in MS-A (~11.5 GPa) and AMS-C (~14 GPa) at 75g of indentation load.

(v) The H/E ratio of MS-D (0.21) and AMS-B (0.28) displays maximum values.